

Geophysical Research Letters[®]



RESEARCH LETTER

10.1029/2024GL113616

Key Points:

- An investigation into how diapycnal mixing and lateral transport modulate nutrient dynamics within an intrathermocline eddy (ITE)
- Elevated nutrient fluxes near the deep chlorophyll maximum suggest ITE enhance nutrient supply in oligotrophic oceans
- ITE modulate mineralization levels through the convergence of sinking particles, enhancing nutrient concentrations

Supporting Information:

Supporting Information may be found in the online version of this article.

Correspondence to:

X. Liu,
liuxin1983@xmu.edu.cn

Citation:

Hu, Z., Liu, Z., Liu, X., Masuda, T., Shiozaki, T., Yamada, H., et al. (2025). Nutrient dynamics modulated by diapycnal mixing and particle sinking pathways within an intrathermocline eddy in the tropical western North Pacific. *Geophysical Research Letters*, 52, e2024GL113616. <https://doi.org/10.1029/2024GL113616>

Received 13 NOV 2024

Accepted 18 JUN 2025

Author Contributions:

Conceptualization: Zhendong Hu, Zhiyu Liu, Xin Liu, Ken Furuya
Data curation: Zhendong Hu, Takako Masuda, Takuhei Shiozaki, Hiroyuki Yamada, Hongyang Lin
Formal analysis: Zhendong Hu
Funding acquisition: Xin Liu, Bangqin Huang, Ken Furuya
Investigation: Xin Liu, Takako Masuda, Hiroyuki Yamada, Ken Furuya
Methodology: Zhendong Hu, Zhiyu Liu, Hiroyuki Yamada, Hongyang Lin
Project administration: Xin Liu, Hiroyuki Yamada, Bangqin Huang, Ken Furuya

© 2025. The Author(s).

This is an open access article under the terms of the [Creative Commons Attribution License](#), which permits use, distribution and reproduction in any medium, provided the original work is properly cited.

Nutrient Dynamics Modulated by Diapycnal Mixing and Particle Sinking Pathways Within an Intrathermocline Eddy in the Tropical Western North Pacific

Zhendong Hu¹ , Zhiyu Liu¹ , Xin Liu^{1,2} , Takako Masuda^{2,3} , Takuhei Shiozaki^{2,4} , Hiroyuki Yamada^{5,6} , Hongyang Lin¹ , Bangqin Huang¹ , and Ken Furuya^{2,7} 

¹State Key Laboratory of Marine Environmental Science, Xiamen University, Xiamen, China, ²Graduate School of Agricultural and Life Sciences, the University of Tokyo, Tokyo, Japan, ³Japan Fisheries Research and Education Agency, Shiozaki, Japan, ⁴Atmosphere and Ocean Research Institute, The University of Tokyo, Kashiwa, Japan, ⁵Meteorological Laboratory, University of the Ryukyus, Okinawa, Japan, ⁶Japan Agency for Marine-Earth Science and Technology (JAMSTEC), Yokosuka, Japan, ⁷Institute of Plankton Eco-engineering, Soka University, Tokyo, Japan

Abstract Oceanic subsurface eddies are believed to potentially impact biogeochemical cycles; however, our understanding remains limited due to sparse in situ observations. This study presents observation of an intrathermocline eddy (ITE) in the tropical western North Pacific and provides a comprehensive analysis of how ITE modulate nutrient dynamics by both diapycnal mixing and lateral transport. Pronounced upward nutrient fluxes were observed within the deep chlorophyll maximum layer due to ITE-induced mixing. Lateral transport directly influenced nutrient concentrations through isopycnal advection and indirectly by regulating the horizontal distribution of sinking particles. The latter likely induced spatial variability in mineralization, which played a dominant role in shaping nutrient enrichment. This study advances our understanding of the biogeochemical impacts of ITE, presenting a new paradigm for their role in nutrient and carbon cycling in oligotrophic oceans.

Plain Language Summary Oceanic subsurface eddies (SSEs) differ from their surface counterparts, exhibiting significant thermohaline anomalies and flow signatures beneath the sea surface. Identifying SSEs from sea surface height is challenging, which makes direct in situ observations difficult. We conducted approximately 36 days of stationary shipboard measurements of a subsurface eddy within the thermocline in the tropical western North Pacific. This provided a comprehensive analysis of the eddy's characteristics, mixing features, and their impacts on nutrient concentrations and fluxes. The observed eddy can regulate the physical advection of water masses, directly impact nutrient concentrations, and indirectly affect them by influencing the mineralization of sinking particles. Additionally, it can modulate turbulent mixing, thereby influencing diapycnal nutrient fluxes. Our findings offer valuable insights into the influence of SSEs on the ocean's biogeochemical cycles.

1. Introduction

The research interest in oceanic subsurface eddies (SSEs) has been increasing. Some SSEs have extended life-spans and are capable of carrying water from their source regions over long distances, therefore they are believed to play a hidden crucial role in the transport of salinity, dissolved oxygen (DO), and nutrients (Auger et al., 2021; Collins et al., 2013; Dengler et al., 2004; Frenger et al., 2018; Hormazabal et al., 2013; Lukas & Santiago-Mandujano, 2001). Isopycnal anomalies of nutrients were usually observed within SSEs and physical transport is thought to be the main cause (Morales et al., 2012; Thomsen et al., 2016). However, other studies suggest that increased biological oxygen consumption within the interiors of SSEs, indicating the potential roles of SSEs in regulating the oceanic biogeochemical cycles (Cornejo D'Ottone et al., 2016; Karstensen et al., 2017). While determining the relative contributions of physical and biogeochemical processes with nutrient concentrations within SSEs is essential, accurately quantifying these contributions through field observations is challenging.

From another perspective, oceanic eddies can also impact the sinking processes of organic particles, thereby mediating global carbon export. Waite et al. (2016) proposed the “wineglass effect” hypothesis to explain particle sorting within anticyclonic eddies. Particle tracking simulations show particles gathering at shallower depths along eddy edges, but field measurements revealing particle concentration near the center at greater depths

Resources: Xin Liu, Takako Masuda, Hiroyuki Yamada, Ken Furuya
Software: Zhendong Hu
Supervision: Zhiyu Liu, Xin Liu, Hiroyuki Yamada, Bangqin Huang, Ken Furuya
Validation: Zhendong Hu, Zhiyu Liu, Xin Liu, Takuhei Shiozaki, Hongyang Lin
Visualization: Zhendong Hu, Xin Liu
Writing – original draft: Zhendong Hu, Xin Liu, Takako Masuda, Hiroyuki Yamada, Hongyang Lin
Writing – review & editing: Zhendong Hu, Zhiyu Liu, Xin Liu, Takako Masuda, Takuhei Shiozaki, Hongyang Lin, Bangqin Huang, Ken Furuya

suggest influences beyond hydrodynamics, with biological factors likely contributing significantly (Samuelson et al., 2012). A few recent studies have explored and suggested the critical impact of mesoscale eddies on particle sinking pathways (Picard et al., 2024; Wang et al., 2022). However, due to limitations in observation techniques and physical understanding, most research currently examines carbon export from a vertical one-dimensional perspective (Henson et al., 2019; Iversen, 2023; Savoye et al., 2006). The physical understanding of particle sinking pathways through eddies remains largely unresolved, which is crucial for advancing our knowledge of the production-export relationship.

The tropical western North Pacific is characterized as an oligotrophic ocean with low biological productivity (Dai et al., 2023; Mackey et al., 1995). Although SSEs have been observed multiple times in this region, all reported SSEs occurred at depths greater than 200 m (Song et al., 2022; Z. Zhang et al., 2019; L. Zhang et al., 2021). The vertical range of SSEs is critical for biogeochemistry, as shallower ones that overlap with the euphotic zone will result in biological production and consumption processes that differ significantly from those at greater depths. Here, we define the main thermocline as where $N > 0.01 \text{ s}^{-1}$, classifying SSEs within the main thermocline as intrathermocline eddies (ITEs) and those deeper than it as subthermocline eddies. We further examine how multiple physical processes regulate nutrient dynamics within an ITE. Specifically, we quantify diapycnal and isopycnal nutrient transport and present a paradigm illustrating how ITEs modulate particle sinking pathways, the latter likely impacting mineralization levels and indirectly influencing nutrient concentrations.

2. Measurements and Methods

2.1. Field Observations and Data Collection

The field observations were conducted aboard the R/V MIRAI in the tropical western North Pacific, specifically at (139.5°E, 5.0°N), spanning approximately 36 days, from 16 May to 20 June 2010 (Figure 1a). Continuous measurements of upper-ocean horizontal velocities were obtained throughout the entire cruise using a shipboard acoustic Doppler current profiler (ADCP). The ADCP velocity data were collected within a depth range of 31.3 m to approximately 665.3 m, with a vertical resolution of 16 m. Temperature, salinity, DO, and chlorophyll-a profiles were obtained using a conductivity-temperature-depth (CTD) system (SBE 911plus) at intervals of 3 hr. The collected data were averaged into 1-day and 1-m bins. In the main text, we present only the velocity, vertical shear, and Richardson number associated with the subinertial component, which dominates as shown in Figure S1 in Supporting Information S1, to better illustrate the main eddy structure. The inertial period at the study site is 5.72 days.

2.2. Nutrients Sample Collection and Analyses

The samples used for the determination of nutrient were collected from 10 to 12 layers within the depth range of 0–200 m. Samples for nutrient analysis were collected in duplicate acid-cleaned polypropylene bottles (50 or 100 ml) and were kept frozen until analyses were conducted on land. The concentrations of nitrate, nitrite, and soluble reactive phosphorus were first examined by a conventional colorimetric method. When the nutrient concentrations were below 0.1 μM , they were analyzed using a supersensitive colorimetric system (detection limit: 121: 3 nM), which comprised an Autoanalyzer II (Technicon) connected to a liquid waveguide capillary cell (LWCC, World Precision Instruments, Inc.) (Hashihama et al., 2009). When the initial nitrate concentration for the nitrate assimilation experiment was below the detection limit, even when the supersensitive colorimetric system was used, the nitrate concentration was assumed to be within the detection limit of 3 nM.

2.3. Diapycnal Diffusivity and Diapycnal Nutrient Fluxes

To estimate diapycnal diffusivity, we combined the Liu17 parameterization (Liu et al., 2017) and the MacKinnon-Gregg parameterization (MacKinnon & Gregg, 2003, 2005), which represents eddy-induced mixing and internal wave-induced mixing, respectively. A detailed elaboration and availability in this study are provided in Text S1 in Supporting Information S1. The diapycnal diffusivity was calculate as follows:

$$\kappa_{\rho} = \kappa_{\text{wave}} + \kappa_{\text{eddy}} = \Gamma \frac{\epsilon_0}{N^2} \left(\frac{N}{N_0} \right) \left(\frac{S_{\text{if}}}{S_0} \right) + \kappa_m (1 + \text{Ri}_{\text{eddy}}/\text{Ri}_c)^{-1}, \quad (1)$$

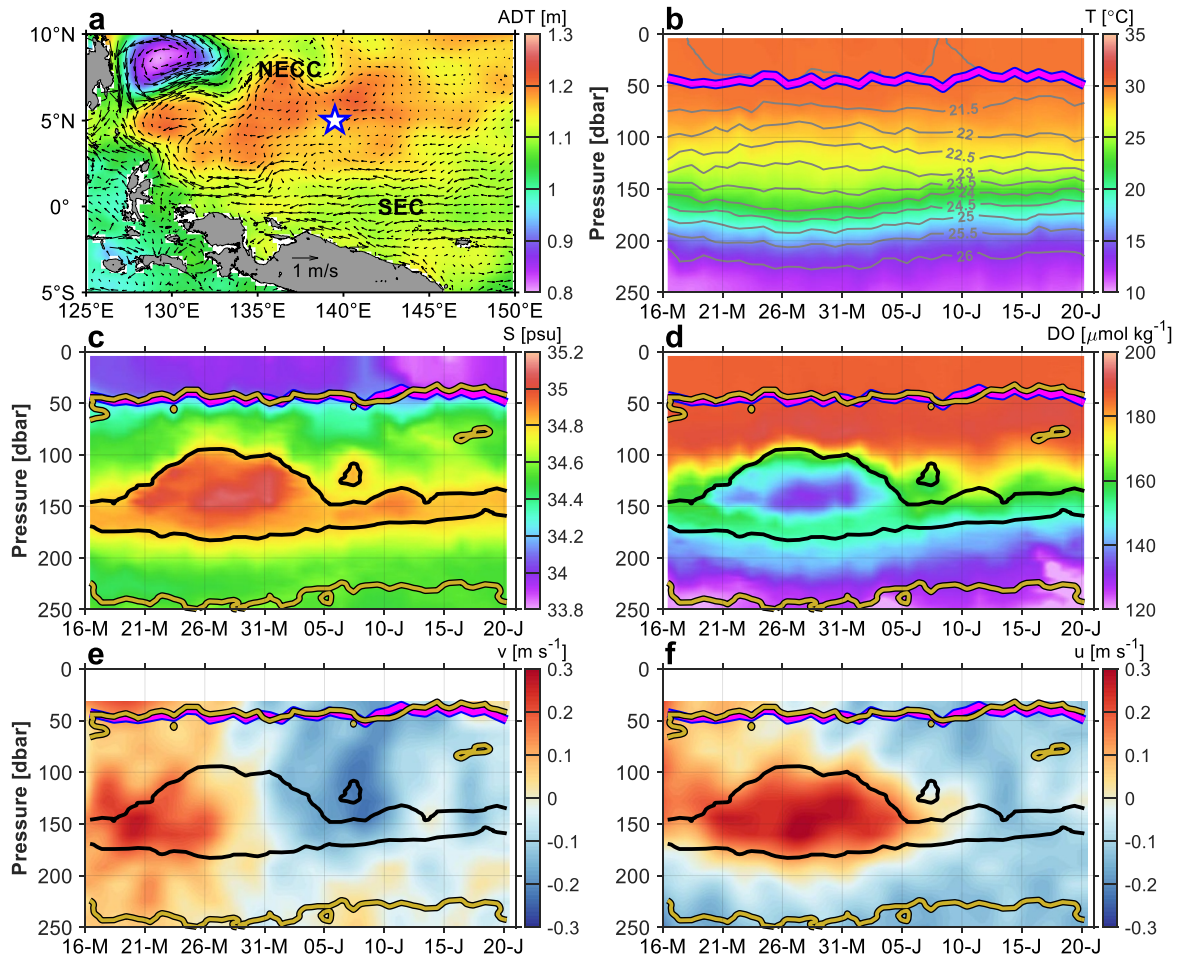


Figure 1. Study region and time series measurements of vertical profiles. (a) Mean absolute dynamic topography (color) and geostrophic velocities (vectors) during the field campaign. NECC, North Equatorial Countercurrent; SEC, South Equatorial Current. The hollow blue pentagon symbol marks the study station. Time series of (b) temperature, (c) salinity, (d) dissolved oxygen, (e) meridional velocity, and (f) zonal velocity. Gray contours in (b) indicate isopycnals from 21 to 26 kg m^{-3} , with an interval of 0.5 kg m^{-3} . Magenta lines in (b–f) indicate the depth of the mixed layer base (defined with the criterion of 0.125 kg m^{-3} greater than the density at 10 m depth). Yellow lines in (c–f) indicate the of $N = 0.01 \text{ s}^{-1}$ contour. Black lines in (c–f) indicate the 34.8 isohalines.

where κ_{wave} and κ_{eddy} denotes the diffusivity resulting from internal wave breaking and eddy-induced shear, respectively. The mixing efficiency Γ is taken as the canonical value of 0.2, assuming a constant ratio between the turbulent energy sink for mixing and viscous dissipation (Gregg et al., 2018; Ivey et al., 2008; Smyth, 2020). N^2 is the squared buoyancy frequency, S_{lf} is the low-frequency, low-mode resolved shear, $S_0 = N_0 = 3 \text{ cph}$, and $\varepsilon_0 = 1.1 \times 10^{-9} \text{ W kg}^{-1}$ (MacKinnon & Gregg, 2005). $\text{Ri}_c = 0.25$ represents the critical value of Ri_{eddy} ($\text{Ri}_{\text{eddy}} = N^2/S_{\text{eddy}}^2$ with S_{eddy}^2 being the squared eddy-induced shear) for eddy-induced shear instability. κ_m representing the (maximum) diffusivity corresponding to a vanishing Ri_{eddy} , given by $\kappa_m = 1.9 \times 10^{-4} \text{ m}^2 \text{ s}^{-1}$ (Liu et al., 2017). The velocity data were first processed using a 1-hr low-pass filter. Then, to obtain S_{lf} , we combined the velocity components from near-inertial, diurnal, semidiurnal and sub-semidiurnal bands to calculate the vertical shear associated with low-frequency, low-mode internal waves. For S_{eddy}^2 , we used the remaining velocity components to calculate the vertical shear associated with eddies. Although shear from large-scale currents may also exist, we do not distinguish it here.

The diapycnal flux for a substance (F_v) consists of both diffusive (F_{diff}) and advective (F_{adv}) components (Du et al., 2017; Spingys et al., 2021), as given by:

$$F_v = F_{\text{diff}} + F_{\text{adv}} = -\kappa_\rho \frac{\partial c}{\partial z} + w_* c, \quad (2)$$

where c represents the concentration of the substance, and $\partial c/\partial z$ represents the vertical gradient of c . The diapycnal velocity w_* is calculated using the equation derived by McDougall (McDougall, 1984, 1987). Neglecting both isopycnal diffusivity and double diffusion, the equation simplifies to:

$$w_* = \frac{1}{N^2} \frac{\partial}{\partial z} (\kappa_\rho \cdot N^2) + \frac{g}{N^2} \left[-\frac{\partial \alpha}{\partial \theta} \kappa_\rho \theta_z^2 - \frac{\partial \alpha}{\partial p} \kappa_\rho \theta_z p_z \right], \quad (3)$$

where α is the thermal expansion coefficient, θ is the potential temperature, and p is the pressure. The subscript z indicates the partial derivative with respect to depth z .

2.4. OFES Output and WOA18 Climatology

To investigate the generation features of ITEs, as well as the modulation of particle sinking dynamics by ITEs, we use the realistic eddy-resolving numerical output (1/10° horizontal resolution) from the Ocean General Circulation Model for the Earth Simulator (OFES) hindcast simulation. Details of the OFES output are available in Masumoto et al. (2004) and Sasaki et al. (2008).

To infer the potential source region of the ITEs and further quantify the isopycnal advection contribution to DO and nutrients, we used climatological data for temperature, salinity, DO, nitrate, and phosphate from the World Ocean Atlas 2018 (WOA18), as compiled by Boyer et al. (2018).

2.5. Particle Sinking Simulations

To gain a fundamental understanding of sinking particle behavior within ITEs, we conduct particle sinking simulations. Following Waite et al. (2016), we assume that the sinking velocity is given by $s = s_0 (\rho_p - \rho) / (\rho_p - \rho_0)$, where ρ_0 is the minimum surface density, s_0 is the base sinking rate at the surface and ρ_p is the particle density. In this case, we used $s_0 = 5 \text{ m d}^{-1}$ and $\rho_p / \rho_0 = 1.006$, while also testing $s_0 = 1 \text{ m d}^{-1}$ and $s_0 = 50 \text{ m d}^{-1}$. These variations did not affect the spatial patterns of horizontal spatial variabilities of sinking particle (not shown), so we presented only the midrange case ($s_0 = 5 \text{ m d}^{-1}$). The sinking velocities were then averaged horizontally. Additionally, we considered the 3D horizontal velocity field from OFES output to assess the impact of ITE-induced lateral transport on particle sinking pathways. Excluding vertical velocity did not alter the overall patterns but removed a few fine-scale patches, highlighting the main features (not shown). To simulate the continuous production of organic particles, virtual sinking particles were released daily at a depth of 10 m, with a horizontal resolution of 0.2°. The initial particle release began at least 100 days before ITE events, allowing the system to stabilize and ensuring that the total particle count remained nearly constant across all depths during ITE events.

3. Results and Discussion

3.1. General Features of the ITE

Altimetry observations indicated that the North Equatorial Counter Current was relatively weak in the northern region adjacent to the study area during the field campaign (Figure 1a). Additionally, the surface geostrophic currents at the study station were exceptionally weak and suggested a lack of surface-intensified eddy activities. However, the time series measurements of vertical profiles revealed the presence of a lens-shaped temperature and density structure within the main thermocline from 18 May to 5 June, characterized by significantly higher salinity and lower DO levels (Figures 1b–1d). This lens-shaped structure closely resembles subsurface-intensified anticyclonic eddies.

Velocity measurements also revealed the presence of subsurface-intensified flow (Figures 1e and 1f). The meridional velocity exhibited an eddy-like flow structure, with initial northward flows transitioning to southward flows later. In contrast, the zonal velocity displayed a predominant eastward flow, indicating that the study station was located at the northern periphery of the eddy. The influence of the subsurface eddy was primarily confined within the main thermocline. Hence, we classify it as an ITE.

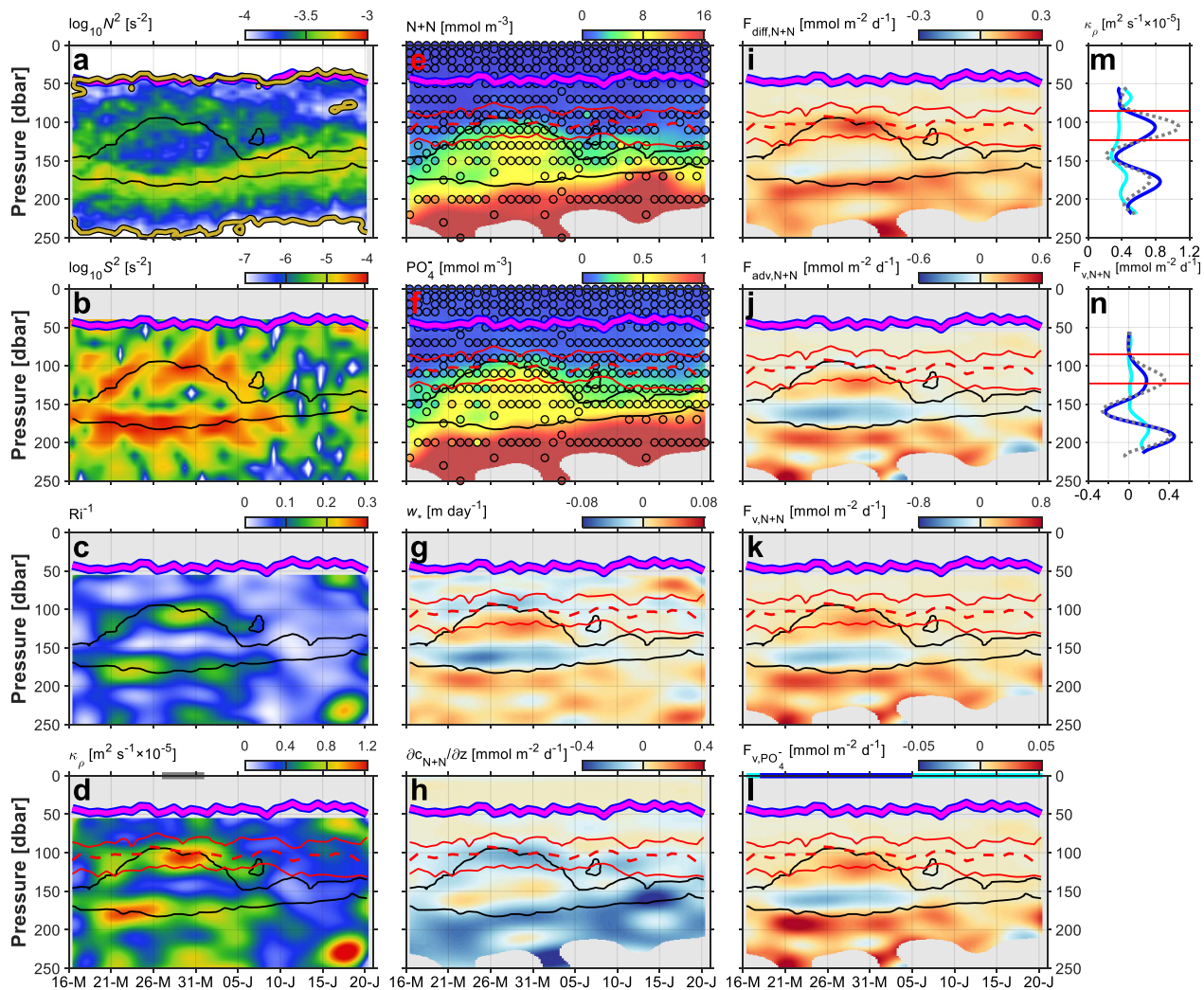


Figure 2. Characteristics of diapycnal mixing and diapycnal fluxes. (a) Squared buoyancy frequency (N^2). (b) Squared shear (S^2). (c) The inverse gradient Richardson number (Ri^{-1}). (d) Diapycnal diffusivity (K_ρ). The gray solid line on the top axis indicates the high mixing event. (e, f) Concentrations of nitrate and phosphate. Both the sampled data points (colored dots) and the corresponding continuous distribution obtained through objective mapping (colored areas) are displayed. (g) Diapycnal velocity. (h) Vertical nitrate gradient. (i, j) Diapycnal nitrate fluxes resulting from diapycnal diffusion (F_{diff}) and diapycnal advection (F_{adv}). (k, l) Total diapycnal fluxes (F_v) of nitrate and phosphate. The red dashed and solid lines in (d–l) indicate the maximum of chlorophyll and the deep chlorophyll maximum (DCM) layer, respectively. The extent of the DCM layer is determined by the depth at which chlorophyll reaches 50% of the time-mean maximum value. The ranges of color bars in (e), (f), (k), and (l) have been scaled by the NP ratio (i.e., 16:1). The cyan solid line and the blue solid line on the top axis of (l) indicate non-intrathermocline eddy (ITE) periods and the ITE event, respectively. (m) Mean profiles of diapycnal diffusivity during non-ITE periods (cyan solid line), the ITE event (blue solid line), and the high mixing event (gray dash line). Red solid lines indicate the mean depths of the DCM layer. (n) Same as (m) but for the diapycnal nitrate flux. No mentioned lines are the same as in Figure 1.

3.2. Elevated Turbulent Mixing and Diapycnal Nutrient Fluxes Within the ITE

The vertical center of the ITE exhibited relatively weaker stratification (Figure 2a), a common characteristic of subsurface-intensified anticyclonic eddies. At the upper and lower sides of the ITE, an increase in vertical shear was observed, resulting in a low Richardson number in this area (Figures 2b and 2c). For clarity, we define the vertical peripheries of the ITE as regions of strong stratification and shear, while the vertical center is characterized by weak stratification and shear. The internal wave-induced mixing acted as a weak background value, and eddy-induced mixing dominated the pattern, as shown in Figure S4 in Supporting Information S1. The strong eddy-induced shear led to elevated diapycnal diffusivity at the vertical peripheries of the ITE (Figure 2d). Throughout the ITE event, enhanced diapycnal diffusivity was observed within the deep chlorophyll maximum (DCM) layer, with a particularly high mixing event detected within the DCM from 27 May to 1 June.

At the study station, nutrient concentrations in the mixed layer were extremely low (Figures 2e and 2f). Notably, a distinct doming of nitrate and phosphate within the ITE indicated nutrient enrichment, with elevated concentrations particularly evident in the lower portion of the DCM. The estimated diapycnal velocity exhibited a sandwich-like structure within the ITE, with positive values at the upper periphery (or lower portion of the DCM) and lower periphery, and negative values in between (Figure 2g). In contrast, during non-ITE periods, the diapycnal velocity remained relatively small. An inverted sandwich-like pattern was observed in the vertical nitrate gradient within the ITE (Figure 2h), with a pronounced negative nitrate gradient at its upper periphery, coinciding with the DCM.

The diapycnal nitrate flux resulting from diapycnal diffusion (F_{diff}) was significantly enhanced at the vertical peripheries of the ITE, coinciding with regions of elevated diapycnal diffusivity and strong nitrate gradients (Figures 2d, 2h, and 2i). In contrast, during non-ITE periods, F_{diff} was approximately one order of magnitude smaller than its enhanced values within the ITE (Figure 2i). The diapycnal nitrate flux resulting from diapycnal advection (F_{adv}) followed a similar pattern, but exhibited a pronounced negative value at the vertical center of the ITE. Both F_{diff} and F_{adv} remained relatively small outside the ITE event but showed substantial increases at the vertical peripheries of the ITE (Figures 2i and 2j). F_{adv} was the dominant contributor to the total diapycnal flux (F_v), highlighting the importance of diapycnal advection, which is often neglected in studies of diapycnal fluxes. However, the peak upward nutrient flux in F_{adv} occurred slightly deeper than that in F_{diff} . The diapycnal fluxes of both nitrate and phosphate exhibited similar patterns, with their ratio closely matching to the canonical NP ratio (i.e., 16:1), though slightly elevated for phosphate (Figures 2k and 2l). Importantly, significant diapycnal fluxes were found within the DCM during the ITE event.

To characterize the variability in diapycnal mixing and diapycnal nitrate fluxes across different periods, we calculated averages for both the ITE event and non-ITE periods and examined the mean profile during the high mixing event (Figures 2m and 2n). We focused on both the mean and maximum diapycnal diffusivity and fluxes within the DCM. The mean diapycnal diffusivity was higher during the ITE event ($6.8 \times 10^{-6} \text{ m}^2 \text{ s}^{-1}$) compared to non-ITE periods ($3.6 \times 10^{-6} \text{ m}^2 \text{ s}^{-1}$). Similarly, the maximum diapycnal diffusivity increased from $3.7 \times 10^{-6} \text{ m}^2 \text{ s}^{-1}$ during non-ITE periods to $7.9 \times 10^{-6} \text{ m}^2 \text{ s}^{-1}$ in the ITE event. During the high mixing event, both the mean and maximum diapycnal diffusivity increased further to $8.8 \times 10^{-6} \text{ m}^2 \text{ s}^{-1}$ and $11 \times 10^{-6} \text{ m}^2 \text{ s}^{-1}$, respectively (Figure 2m). The diapycnal nitrate flux within the DCM also exhibited substantial variability. Mean fluxes increased nearly eightfold, from $0.013 \text{ mmol m}^{-2} \text{ d}^{-1}$ during non-ITE periods to $0.10 \text{ mmol m}^{-2} \text{ d}^{-1}$ in the ITE event. Maximum fluxes followed a similar pattern, rising from $0.027 \text{ mmol m}^{-2} \text{ d}^{-1}$ without ITE to $0.18 \text{ mmol m}^{-2} \text{ d}^{-1}$ during the ITE event. Consequently, during the ITE event, diapycnal nutrient fluxes within the DCM were enhanced by an order of magnitude compared to non-ITE periods, with even more pronounced increases during the high mixing event, where the mean flux reached $0.20 \text{ mmol m}^{-2} \text{ d}^{-1}$ and the maximum peaked at $0.35 \text{ mmol m}^{-2} \text{ d}^{-1}$ (Figure 2n).

We further compared the diapycnal nitrate fluxes from this study with previously reported values from the tropical and subtropical Pacific and its marginal seas (detailed comparisons are provided in Text S2 and Table S1 in Supporting Information S1). Our results show that during non-ITE periods, diapycnal nitrate fluxes align with typical values observed in the tropical and subtropical Pacific (Fernández-Castro et al., 2015; Yuan et al., 2023a, 2023b) but lower than those reported in the South China Sea (Du et al., 2017). However, during ITE and high mixing events, diapycnal nitrate fluxes reach levels comparable to those at high mixing stations in the tropical and subtropical Pacific (Fernández-Castro et al., 2015; Yuan et al., 2023a). Notably, during the ITE event, flux levels resemble those found in the South China Sea (Du et al., 2017) and increase further during the high mixing event. This study highlights the role of ITEs in enhancing nutrient supply in oligotrophic oceans.

3.3. Nutrients Enrichment in the ITE by Mineralization of Aggregated Sinking Particles

Significant anomalies in both DO and nutrient concentrations were observed with the ITE, with three main processes identified as the potential mechanisms: (a) heaving (vertical movements, i.e., rising and sinking) or stretching (deformations, i.e., compressing and expanding) of isopycnals; (b) physical advection of solutes along the isopycnal surfaces; and (c) biogeochemical processes associated with the production and mineralization through biological activities.

The doming of isopycnals in the upper part of the ITE may contribute to the observed nutrient enhancement (Figures 1b, 2e, and 2f), but the extremum values of DO and nutrients exhibit remarkable anomalies along the

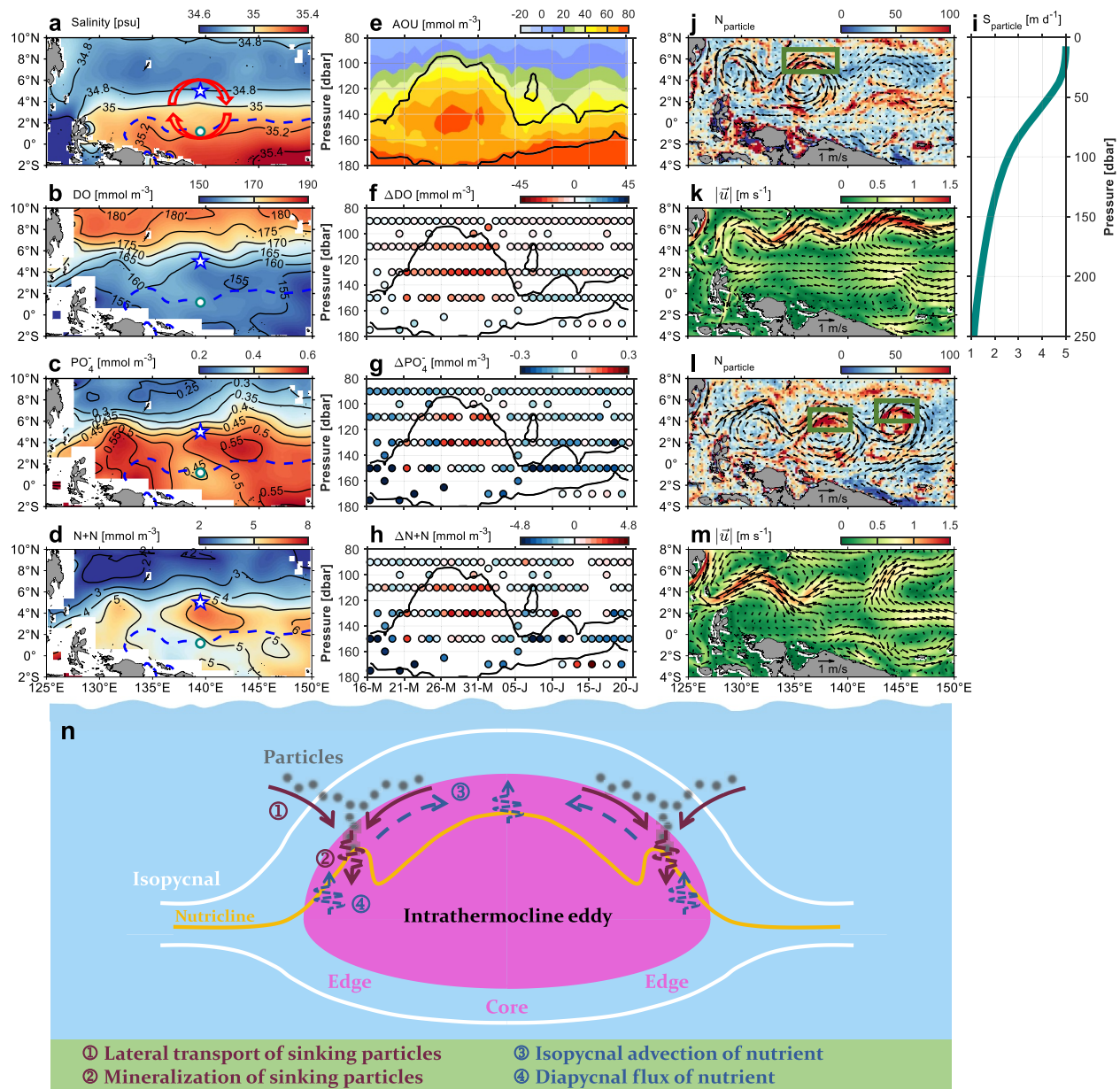


Figure 3. Results from (a–h) isopycnal analysis and (i–m) particle sinking simulations. Climatological distributions of (a) salinity, (b) dissolved oxygen (DO), (c) phosphate, and (d) nitrate on the 23.4 kg m^{-3} isopycnal surface. Black contours represent the corresponding contours for each variable, and blue dashed lines indicate the 35.14 isohaline. The hollow blue pentagon symbol indicates the location of the study station. (e) Time series of apparent oxygen utilization. Biogeochemical contributions for (f) DO, (g) phosphate, and (h) nitrate. The color bar ranges in (f–h) have been scaled by the Redfield ratio (i.e., $\text{O}_2:\text{P}:\text{N} = 150:1:16$). Black lines in (e–h) indicate the 34.8 isohalines. (i) Particle sinking speed used in simulations. (j) Number of particles within per $0.2^\circ \times 0.2^\circ$ horizontal grid and per 100–200 m vertical depth range (color) and horizontal velocities from Ocean General Circulation Model for the Earth Simulator (OFES) (vectors) at 150 m depth on 5 January 2008. (k) Horizontal velocities from OFES at the surface (vectors) and their magnitude (color) on 5 January 2008. (l) Same as (j) but on 23 February 2010. (m) Same as (k) but on 23 February 2010. (n) Schematic of particle and nutrient dynamics within an intrathermocline eddy.

isopycnal surfaces (Figures 1d, 2e, and 2f), suggesting that the heaving or stretching of isopycnals cannot account for these patterns. Additionally, vertical velocity driven by mesoscale ocean flows produces minimal diapycnal flux; its main effect is to change the depth of isopycnals. Therefore, the effect of mesoscale vertical velocity within the ITE, which changes isopycnal depth, is already included here.

To better understand how isopycnal advection impacts nutrient concentrations with ITE, it is essential to first identify the most likely source region of the ITE. Previous studies have shown that SSEs can propagate westward

over long distances, as seen in the Mediterranean outflow eddies and the California undercurrent eddies (Collins et al., 2013; Frenger et al., 2018; Lukas & Santiago-Mandujano, 2001). However, OFES output reveals that ITEs in the tropical western North Pacific are generated locally, with only limited westward propagation after their formation (Figures S5 and S6 in Supporting Information S1). Additionally, the radius of well-defined ITEs is approximately 250 km, which closely matches the local first baroclinic Rossby radius of deformation (around 230 km, according to Chelton et al., 1998). The absence of ITEs propagating from distant eastern locations is further supported by velocity field at the surface and at a depth of 150 m from OFES output over 20 years (not shown).

As SSEs typically induce notable anomalies in salinity, DO, and other tracers along the isopycnals by eddy-induced trapping and transport, examining the distribution of these tracers along the isopycnals is an effective method to infer the source region of the SSEs (Lukas & Santiago-Mandujano, 2001; Z. Zhang et al., 2015). We primarily focus on the transport of water masses along isopycnal surfaces, treating salinity as a conservative tracer. Consequently, the isohaline along the isopycnal surface serves as a key indicator of the potential source region, with the climatological data set from WOA18 used here. Specifically, the 35.14 isohaline (representing the salinity at the vertical center of the ITE) on the 23.4 kg m^{-3} isopycnal surface (the density at the vertical center of the ITE, approximately 150 m depth) suggests the potential source region for the observed high salinity water at the vertical center of the ITE (Figure 3a). A strong meridional salinity gradient is observed near the study station, with the 35.14 isohaline marking the potential source region to the south of the station. Given the strong eastward flow throughout the entire ITE event (Figure 1f) and the ITEs' horizontal radius of approximately 250 km, we can infer the approximate position of the ITE, as shown by the red rotational arrow in Figure 3a. Thus, the observed saltier water within the ITE was advected approximately 400 km south of the study station. Moreover, the saltier water within the ITE was identified as South Pacific Tropic Water, characterized by subsurface waters exhibiting with a local maximum salinity in the tropic and South Pacific subtropic oceans (Qu et al., 2013).

The distribution of DO exhibited a clear meridional variation, with low DO concentrations observed at the source region (Figure 3b). However, significantly lower DO concentrations ($\sim 135 \text{ mmol m}^{-3}$) were found at the vertical center of the ITE (Figure 1d). Additionally, higher nitrate concentrations ($\sim 8.1 \text{ mmol m}^{-3}$) and phosphate concentrations ($\sim 0.55 \text{ mmol m}^{-3}$) were observed in the vertical center of the ITE (Figures 2e and 2f), as compared to those at the source region (Figures 3c and 3d). Moreover, higher apparent oxygen utilization was noted within the ITE, indicating active local biological consumption of DO (Figure 3e). Therefore, the physical advection of solutes along the isopycnal surfaces alone cannot account for the observed significantly lower DO and higher nutrients within the ITE.

Next, we will discuss the contribution of biogeochemistry processes by removing the physical isopycnal advection contribution from the observed values. Given the limited meridional migration of ITEs after their formation and the absence of ITEs propagating from distant regions, as indicated by OFES output, we assume no net meridional migration of source water. Thus, for each water sample, the source location is defined as the intersection of the isohaline lines (derived from the observed salinity values on each isopycnal surface) with the 139.5°E meridian. For example, the green open dot in Figures 3a–3d represents the source location for the water sample with a density of 23.4 kg m^{-3} and a salinity of 35.14. The WOA18 climatology of the source water defines the physical advection contribution along isopycnals, with the remaining value (after subtracting the physical advection contribution) from the water samples representing the biogeochemical contribution.

The biogeochemical contributions are shown in Figures 3f–3h. DO depletion of and nutrient enrichment in the upper ITE were significant, with the ratio of these differences aligning with the Redfield ratio (i.e., $\text{O}_2\text{:P:N} = 150\text{:1:16}$). This suggests that mineralization, which decomposes organic matter and consumes DO to produce nutrients, likely have dominated the observed significantly lower DO and higher nutrient concentrations within the ITE.

However, why did more energetic mineralization occur within ITE? A previous study indicated that eddy-induced horizontal advection can modulate particle sinking dynamics, causing horizontal displacement and convergence/divergence of sinking particles (Waite et al., 2016). Inspired by this, we propose a hypothesis that the ITE may aggregate organic sinking particles in specific areas, thus enhancing local mineralization. To verify this hypothesis, we conducted simulations to investigate how ITE-induced flows modulate the distributions of sinking particles and, in turn, affect mineralization (see details in Section 2.5). The OFES output provides a realistic

numerical simulation that is also dynamically self-consistent, making it a valuable tool for this analysis. An example of an ITE identified in the OFES output exhibits a similar vertical extent and structure in salinity, density, shear, and stratification (Figure S7 in Supporting Information S1) compared to the observed ITE (Figures 1 and 2). Therefore, the OFES output is well suited for studying particle sinking dynamics within ITEs. Significant eddy-induced flows were clearly observed at 150 m (Figures 3j and 3l), while no obvious eddy-like flow features were present at the surface (Figures 3k and 3m), confirming that these eddies are ITEs. Notably, higher particle concentrations were found at the peripheries of ITEs (Figures 3j and 3l), and these high-concentration features can persist for over a month until the ITEs lose coherence or dissipate (Figures S8 and S9 in Supporting Information S1). It is important to recall that the study station was located at the northern periphery of the ITE (Figure 3a), and the released sinking particles were found to accumulated in similar locations with strong eastward flows (green boxes in Figures 3j and 3l).

It can be speculated that the observed ITE accumulated organic particles at its horizontal peripheries. These accumulated particles likely consumed more DO and produced an abundance of nutrients through mineralization. Previous studies have shown a greater biological consumption of DO within the interiors of ITEs, suggesting the potential roles of ITEs in regulating the oceanic biogeochemical cycles (Cornejo D'Ottone et al., 2016; Karstensen et al., 2017). Here, we offer a new explanation: increased mineralization due to particle aggregation by ITE activities are likely contribute to the high biological consumption of DO with ITEs.

4. Conclusion and Implications

Figure 3n illustrates nutrient dynamics driven by multiple physical processes within an ITE. In summary, organic sinking particles accumulate at the horizontal peripheries of the ITE through horizontal transport, where their mineralization increases local nutrient concentrations. The released nutrients are then redistributed along isopycnals via physical advection and enhance nutrient supply to the DCM through ITE-induced diapycnal mixing.

Parameterization-based estimates of diapycnal diffusivity indicate enhanced mixing during the ITE event, with an order-of-magnitude increase in diapycnal nutrient fluxes. These fluxes exceed the normal levels in the oligotrophic Pacific, highlighting ITEs as a significant nutrient source in oligotrophic oceans. Further studies based on microstructure measurements are needed to provide the direct and universal evidence of ITE-induced mixing and diapycnal nutrient fluxes.

A paradigm illustrating the effect of ITEs on particle sinking pathways was presented, offering new insights into the horizontal displacement of production and export. Despite the evident importance of lateral transport for organic particles, its impact has not been incorporated in the production-export relationship due to limited physical-biogeochemical understanding. Further research is needed to uncover how multi-scale oceanic processes modulate particle sinking dynamics, thus establishing a first-order understanding of the physical advection effect.

Data Availability Statement

The satellite altimeter data were sourced from the Copernicus Marine Data Store (https://data.marine.copernicus.eu/product/SEALEVEL_GLO_PHY_L4_MY_008_047/description). The World Ocean Atlas 2018 data were accessed from the National Centers for Environmental Information (<https://www.ncei.noaa.gov/access/world-ocean-atlas-2018>). The OFES version 1 data were obtained from the Japan Agency for Marine-Earth Science and Technology (JAMSTEC) website (<https://www.jamstec.go.jp/ofes/ofes.html>). The observational data used in this study are available from JAMSTEC's data archive (https://www.godac.jamstec.go.jp/darwin_cruise/view/meta-data?key=MR10-03_leg2&lang=en).

Acknowledgments

This work was supported by the National Key Research and Development Program of China (Grant 2023YFF0805003, 2023YFE0126700, and 2022YFA1003804), and the Natural Science Foundation of Fujian Province of China (Grant 2021J02005). We thank the crew of the R/V MIRAI for their assistance in data collection. Marcus Dengler, Ze Chen, and Lizhen Lin are thanked for their helpful discussions.

References

- Auger, P. A., Bento, J. P., Hormazabal, S., Morales, C. E., & Bustamante, A. (2021). Mesoscale variability in the boundaries of the oxygen minimum zone in the eastern South Pacific: Influence of intrathermocline eddies. *Journal of Geophysical Research: Oceans*, 126(2), e2019JC015272. <https://doi.org/10.1029/2019jc015272>
- Boyer, T. P., Garcia, H. E., Locarnini, R. A., Zweng, M. M., Mishonov, A. V., Reagan, J. R., et al. (2018). World ocean atlas.
- Chelton, D. B., de Szoeke, R. A., Schlax, M. G., El Naggar, K., & Siwertz, N. (1998). Geographical variability of the first baroclinic Rossby radius of deformation. *Journal of Physical Oceanography*, 28(3), 433–460. [https://doi.org/10.1175/1520-0485\(1998\)028<0433:gvotfb>2.0.co;2](https://doi.org/10.1175/1520-0485(1998)028<0433:gvotfb>2.0.co;2)
- Collins, C. A., Margolina, T., Rago, T. A., & Ivanov, L. (2013). Looping RAFOS floats in the California current system. *Deep Sea Research Part II: Topical Studies in Oceanography*, 85, 42–61. <https://doi.org/10.1016/j.dsr2.2012.07.027>

- Cornejo D'Ottone, M., Bravo, L., Ramos, M., Pizarro, O., Karstensen, J., Gallegos, M., et al. (2016). Biogeochemical characteristics of a long-lived anticyclonic eddy in the eastern South Pacific Ocean. *Biogeosciences*, 13(10), 2971–2979. <https://doi.org/10.5194/bg-13-2971-2016>
- Dai, M., Luo, Y., Achterberg, E. P., Browning, T. J., Cai, Y., Cao, Z., et al. (2023). Upper Ocean biogeochemistry of the oligotrophic North Pacific subtropical gyre: From nutrient sources to carbon export. *Reviews of Geophysics*, 61(3), e2022RG000800. <https://doi.org/10.1029/2022rg000800>
- Dengler, M., Schott, F. A., Eden, C., Brandt, P., Fischer, J., & Zantopp, R. J. (2004). Break-up of the Atlantic deep western boundary current into eddies at 8° S. *Nature*, 432(7020), 1018–1020. <https://doi.org/10.1038/nature03134>
- Du, C., Liu, Z., Kao, S.-J., & Dai, M. (2017). Diapycnal fluxes of nutrients in an oligotrophic oceanic regime: The south China Sea. *Geophysical Research Letters*, 44(22), 11510–11518. <https://doi.org/10.1002/2017gl074921>
- Fernández-Castro, B., Mourinho-Carballido, B., Marañón, E., Chouciño, P., Gago, J., Ramírez, T., et al. (2015). Importance of salt fingering for new nitrogen supply in the oligotrophic ocean. *Nature Communications*, 6(1), 8002. <https://doi.org/10.1038/ncomms9002>
- Frenger, I., Bianchi, D., Stühenberg, C., Oschlies, A., Dunne, J., Deutsch, C., et al. (2018). Biogeochemical role of subsurface coherent eddies in the Ocean: Tracer Cannonballs, hypoxic storms, and microbial stewpots? *Global Biogeochemical Cycles*, 32(2), 226–249. <https://doi.org/10.1002/2017gb005743>
- Gregg, M. C., Asaro, E. A., Riley, J. J., & Kunze, E. (2018). Mixing efficiency in the Ocean. *Annual Review of Marine Science*, 10(1), 443–473. <https://doi.org/10.1146/annurev-marine-121916-063643>
- Hashihama, F., Furuya, K., Kitajima, S., Takeda, S., Takemura, T., & Kanda, J. (2009). Macro-scale exhaustion of surface phosphate by dinitrogen fixation in the western North Pacific. *Geophysical Research Letters*, 36(3), L03610. <https://doi.org/10.1029/2008gl036866>
- Henson, S., Le Moigne, F., & Giering, S. (2019). Drivers of carbon export efficiency in the global ocean. *Global Biogeochemical Cycles*, 33(7), 891–903. <https://doi.org/10.1029/2018gb006158>
- Hormazabal, S., Combes, V., Morales, C. E., Correa-Ramirez, M. A., Di Lorenzo, E., & Nuñez, S. (2013). Intrathermocline eddies in the coastal transition zone off central Chile (31°–41°S). *Journal of Geophysical Research: Oceans*, 118(10), 4811–4821. <https://doi.org/10.1002/jgrc.20337>
- Iversen, M. H. (2023). Carbon export in the ocean: A biologist's perspective. *Annual Review of Marine Science*, 15(1), 357–381. <https://doi.org/10.1146/annurev-marine-032122-035153>
- Ivey, G. N., Winters, K. B., & Koseff, J. R. (2008). Density stratification, turbulence, but how much mixing? *Annual Review of Fluid Mechanics*, 40(1), 169–184. <https://doi.org/10.1146/annurev-fluid.39.050905.110314>
- Karstensen, J., Schütte, F., Pietri, A., Krahmann, G., Fiedler, B., Grundle, D., et al. (2017). Upwelling and isolation in oxygen-depleted anticyclonic modewater eddies and implications for nitrate cycling. *Biogeosciences*, 14(8), 2167–2181. <https://doi.org/10.5194/bg-14-2167-2017>
- Liu, Z., Lian, Q., Zhang, F., Wang, L., Li, M., Bai, X., et al. (2017). Weak thermocline mixing in the north Pacific low-latitude western boundary current system. *Geophysical Research Letters*, 44(20), 10530–10539. <https://doi.org/10.1002/2017gl075210>
- Lukas, R., & Santiago-Mandujano, F. (2001). Extreme water mass anomaly observed in the Hawaii ocean time-series. *Geophysical Research Letters*, 28(15), 2931–2934. <https://doi.org/10.1029/2001gl013099>
- Mackey, D. J., Parslow, J., Higgins, H. W., Griffiths, F. B., & O'Sullivan, J. E. (1995). Plankton productivity and biomass in the western equatorial Pacific: Biological and physical controls. *Deep Sea Research Part II: Topical Studies in Oceanography*, 42(2), 499–533. [https://doi.org/10.1016/0967-0645\(95\)00038-r](https://doi.org/10.1016/0967-0645(95)00038-r)
- MacKinnon, J. A., & Gregg, M. C. (2003). Mixing on the late-summer new England shelf—Solibores, shear, and stratification. *Journal of Physical Oceanography*, 33(7), 1476–1492. [https://doi.org/10.1175/1520-0485\(2003\)033<1476:motlne>2.0.co;2](https://doi.org/10.1175/1520-0485(2003)033<1476:motlne>2.0.co;2)
- MacKinnon, J. A., & Gregg, M. C. (2005). Spring mixing: Turbulence and internal waves during restratification on the new England shelf. *Journal of Physical Oceanography*, 35(12), 2425–2443. <https://doi.org/10.1175/jpo2821.1>
- Masumoto, Y., Sasaki, H., Kagimoto, T., Komori, N., Ishida, A., Sasai, Y., et al. (2004). A fifty-year eddy-resolving simulation of the world ocean: Preliminary outcomes of OFES (OGCM for the Earth Simulator). *Journal of Earth Simulator*, 1, 35–56.
- McDougall, T. J. (1984). The relative roles of diapycnal and isopycnal mixing on subsurface water mass conversion. *Journal of Physical Oceanography*, 14(10), 1577–1589. [https://doi.org/10.1175/1520-0485\(1984\)014<1577:troda>2.0.co;2](https://doi.org/10.1175/1520-0485(1984)014<1577:troda>2.0.co;2)
- McDougall, T. J. (1987). Thermobaricity, cabbeling, and water-mass conversion. *Journal of Geophysical Research*, 92(C5), 5448–5464.
- Morales, C. E., Hormazabal, S., Correa-Ramirez, M., Pizarro, O., Silva, N., Fernandez, C., et al. (2012). Mesoscale variability and nutrient-phytoplankton distributions off central-southern Chile during the upwelling season: The influence of mesoscale eddies. *Progress in Oceanography*, 104, 17–29. <https://doi.org/10.1016/j.pocean.2012.04.015>
- Picard, T., Gula, J., Fablet, R., Collin, J., & Mémer, L. (2024). Predicting particle catchment areas of deep-ocean sediment traps using machine learning. *Ocean Science*, 20(5), 1149–1165. <https://doi.org/10.5194/os-20-1149-2024>
- Qu, T., Gao, S., & Fine, R. A. (2013). Subduction of South Pacific tropical water and its equatorward pathways as shown by a simulated passive tracer. *Journal of Physical Oceanography*, 43(8), 1551–1565. <https://doi.org/10.1175/jpo-d-12-0180.1>
- Samuelson, A., Hjøllø, S. S., Johannessen, J. A., & Patel, R. (2012). Particle aggregation at the edges of anticyclonic eddies and implications for distribution of biomass. *Ocean Science*, 8(3), 389–400. <https://doi.org/10.5194/os-8-389-2012>
- Sasaki, H., Nonaka, M., Masumoto, Y., Sasai, Y., Uehara, H., & Sakuma, H. (2008). An eddy-resolving hindcast simulation of the quasiglobal ocean from 1950 to 2003 on the Earth Simulator. In *High resolution numerical modelling of the atmosphere and ocean* (pp. 157–185). Springer
- Savoye, N., Benitez-Nelson, C., Burd, A. B., Cochran, J. K., Charette, M., Buesseler, K. O., et al. (2006). 234Th sorption and export models in the water column: A review. *Marine Chemistry*, 100(3–4), 234–249. <https://doi.org/10.1016/j.marchem.2005.10.014>
- Smyth, W. D. (2020). Marginal instability and the efficiency of Ocean Mixing. *Journal of Physical Oceanography*, 50(8), 2141–2150. <https://doi.org/10.1175/jpo-d-20-0083.1>
- Song, W., Zhang, L., & Hu, D. (2022). Observed subsurface lens-like features east of the Philippines. *Deep Sea Research Part I: Oceanographic Research Papers*, 190, 103901. <https://doi.org/10.1016/j.dsr.2022.103901>
- Spingys, C. P., Williams, R. G., Tuerena, R. E., Naveira Garabato, A., Vic, C., Forryan, A., & Sharples, J. (2021). Observations of nutrient supply by mesoscale eddy stirring and small-scale turbulence in the oligotrophic north Atlantic. *Global Biogeochemical Cycles*, 35(12), e2021GB007200. <https://doi.org/10.1029/2021gb007200>
- Thomsen, S., Kanzow, T., Krahmann, G., Greatbatch, R. J., Dengler, M., & Lavik, G. (2016). The formation of a subsurface anticyclonic eddy in the Peru-Chile Undercurrent and its impact on the near-coastal salinity, oxygen, and nutrient distributions. *Journal of Geophysical Research: Oceans*, 121(1), 476–501. <https://doi.org/10.1002/2015jc010878>
- Waite, A. M., Stemann, L., Guidi, L., Calil, P. H. R., Hogg, A. M. C., Feng, M., et al. (2016). The wineglass effect shapes particle export to the deep ocean in mesoscale eddies. *Geophysical Research Letters*, 43(18), 9791–9800. <https://doi.org/10.1002/2015gl066463>
- Wang, L., Gula, J., Collin, J., & Mémer, L. (2022). Effects of mesoscale dynamics on the path of fast-sinking particles to the deep ocean: A modeling study. *Journal of Geophysical Research: Oceans*, 127(7), e2022JC018799. <https://doi.org/10.1029/2022jc018799>

- Yuan, Z., Browning, T. J., Du, C., Shen, H., Wang, L., Ma, Y., et al. (2023a). Enhanced phosphate consumption stimulated by nitrogen fixation within a cyclonic eddy in the northwest pacific. *Journal of Geophysical Research: Oceans*, 128(11), e2023JC019947. <https://doi.org/10.1029/2023jc019947>
- Yuan, Z., Browning, T. J., Zhang, R., Wang, C., Du, C., Wang, Y., et al. (2023b). Potential drivers and consequences of regional phosphate depletion in the western subtropical North Pacific. *Limnology and Oceanography Letters*, 8(3), 509–518. <https://doi.org/10.1002/lol2.10314>
- Zhang, L., Hui, Y., Qu, T., & Hu, D. (2021). Seasonal variability of subthermocline eddy kinetic energy east of the Philippines. *Journal of Physical Oceanography*, 51(3), 685–699. <https://doi.org/10.1175/jpo-d-20-0101.1>
- Zhang, Z., Li, P., Xu, L., Li, C., Zhao, W., Tian, J., & Qu, T. (2015). Subthermocline eddies observed by rapid-sampling Argo floats in the subtropical northwestern Pacific Ocean in Spring 2014. *Geophysical Research Letters*, 42(15), 6438–6445. <https://doi.org/10.1002/2015gl064601>
- Zhang, Z., Liu, Z., Richards, K., Shang, G., Zhao, W., Tian, J., et al. (2019). Elevated diapycnal mixing by a subthermocline eddy in the western equatorial pacific. *Geophysical Research Letters*, 46(5), 2628–2636. <https://doi.org/10.1029/2018gl081512>

References From the Supporting Information

- Bretherton, F. P., Davis, R. E., & Fandry, C. (1976). A technique for objective analysis and design of oceanographic experiments applied to MODE-73. In *Deep Sea research and oceanographic abstracts*. Elsevier.
- de Lavergne, C., Vic, C., Madec, G., Roquet, F., Waterhouse, A. F., Whalen, C. B., et al. (2020). A parameterization of local and remote tidal mixing. *Journal of Advances in Modeling Earth Systems*, 12(5), e2020MS002065. <https://doi.org/10.1029/2020ms002065>
- Gregg, M. C., Sanford, T. B., & Winkel, D. P. (2003). Reduced mixing from the breaking of internal waves in equatorial waters. *Nature*, 422(6931), 513–515. <https://doi.org/10.1038/nature01507>
- Klymak, J. M., Moum, J. N., Nash, J. D., Kunze, E., Giron, J. B., Carter, G. S., et al. (2006). An estimate of tidal energy lost to turbulence at the Hawaiian ridge. *Journal of Physical Oceanography*, 36(6), 1148–1164. <https://doi.org/10.1175/jpo2885.1>
- Liang, C.-R., Chen, G.-Y., & Shang, X.-D. (2017). Observations of the turbulent kinetic energy dissipation rate in the upper central south China Sea. *Ocean Dynamics*, 67(5), 597–609. <https://doi.org/10.1007/s10236-017-1051-6>
- Liang, C.-R., Shang, X.-D., Qi, Y.-F., Chen, G.-Y., & Yu, L.-H. (2018). Assessment of fine-scale parameterizations at low latitudes of the North Pacific. *Scientific Reports*, 8(1), 10281. <https://doi.org/10.1038/s41598-018-28554-z>
- Liang, C.-R., Shang, X.-D., Qi, Y.-F., Chen, G.-Y., & Yu, L.-H. (2019). Enhanced diapycnal mixing between water masses in the western equatorial pacific. *Journal of Geophysical Research: Oceans*, 124(11), 8102–8115. <https://doi.org/10.1029/2019jc015463>
- Liang, C.-R., Shang, X.-D., Qi, Y.-F., Chen, G.-Y., & Yu, L.-H. (2021). A modified finescale parameterization for turbulent mixing in the western equatorial pacific. *Journal of Physical Oceanography*, 51(4), 1133–1143. <https://doi.org/10.1175/jpo-d-20-0205.1>
- Moum, J. N., Lien, R. C., Perlin, A., Nash, J. D., Gregg, M. C., & Wiles, P. J. (2009). Sea surface cooling at the Equator by subsurface mixing in tropical instability waves. *Nature Geoscience*, 2(11), 761–765. <https://doi.org/10.1038/ngeo657>
- Palmer, M. R., Rippeth, T. P., & Simpson, J. H. (2008). An investigation of internal mixing in a seasonally stratified shelf sea. *Journal of Geophysical Research*, 113(C12), C12005. <https://doi.org/10.1029/2007jc004531>
- Rudnick, D. L., Boyd, T. J., Brainard, R. E., Carter, G. S., Egbert, G. D., Gregg, M. C., et al. (2003). From tides to mixing along the Hawaiian ridge. *Science*, 301(5631), 355–357. <https://doi.org/10.1126/science.1085837>
- Shang, X. D., Liang, C. R., & Chen, G. Y. (2017). Spatial distribution of turbulent mixing in the upper ocean of the South China Sea. *Ocean Science*, 13(3), 503–519. <https://doi.org/10.5194/os-13-503-2017>
- Smyth, W. D., & Moum, J. N. (2013). Marginal instability and deep cycle turbulence in the eastern equatorial Pacific Ocean. *Geophysical Research Letters*, 40(23), 6181–6185. <https://doi.org/10.1002/2013gl058403>
- Sun, H., Yang, Q., & Tian, J. (2018). Microstructure measurements and finescale parameterization assessment of turbulent mixing in the northern South China Sea. *Journal of Oceanography*, 74(5), 485–498. <https://doi.org/10.1007/s10872-018-0474-0>
- van der Lee, E. M., & Umlauf, L. (2011). Internal wave mixing in the Baltic Sea: Near-inertial waves in the absence of tides. *Journal of Geophysical Research*, 116(C10), C10016. <https://doi.org/10.1029/2011jc007072>
- Whalen, C. B., MacKinnon, J. A., & Talley, L. D. (2018). Large-scale impacts of the mesoscale environment on mixing from wind-driven internal waves. *Nature Geoscience*, 11(11), 842–847. <https://doi.org/10.1038/s41561-018-0213-6>
- Xie, X. H., Cuypers, Y., Bouruet-Aubertot, P., Ferron, B., Pichon, A., Lourenço, A., & Cortes, N. (2013). Large-amplitude internal tides, solitary waves, and turbulence in the central Bay of Biscay. *Geophysical Research Letters*, 40(11), 2748–2754. <https://doi.org/10.1002/grl.50533>
- Yang, Q., Zhao, W., Li, M., & Tian, J. (2014). Spatial structure of turbulent mixing in the northwestern pacific ocean. *Journal of Physical Oceanography*, 44(8), 2235–2247. <https://doi.org/10.1175/jpo-d-13-0148.1>